Manipulation and Characterization of Aperiodical Graphene Structures Created in a Two-Dimensional Electron Gas

Shiyong Wang, Liang Z. Tan, Weihua Wang, Steven G. Louie, and Nian Lin

Phys. Rev. Lett. **113**, 196803 — Published 7 November 2014

DOI: 10.1103/PhysRevLett.113.196803

Manipulation and Characterization of Aperiodic Structures in Artificial Graphene Created in Two-Dimensional Electron Gas

Shiyong Wang[1], Liang Z. Tan[2], Weihua Wang[1], Steven G. Louie[2,3], Nian Lin[1]*

[1]*Department of Physics, The Hong Kong University of Science and Technology, Hong Kong, China*

[2]*Department of Physics, University of California, Berkeley, CA 94720-7300, USA, and Material Sciences Division, Lawrence Berkeley National Laboratory, Berkeley, CA94720, USA*

[3]*Institute for Advanced Study, Hong Kong University of Science and Technology, Hong Kong, China*

Abstract

We demonstrate that Dirac fermions can be created and manipulated in two-dimensional electron gas (2DEG). Using a cryogenic scanning tunneling microscope, we arranged coronene molecules one by one on a Cu(111) surface to construct artificial graphene nanoribbons with perfect zigzag (ZGNRs) or arm-chair (AGNRs) edges and confirmed that new states localized along the edges emerge only in the ZGNRs. We further made and studied several typical defects, such as single vacancies, Stone-Wales defects and dislocation lines, and found that all these defects introduce localized states at or near the Dirac point in the quasiparticle spectra. Our results confirm that artificial systems built on 2DEG provide rigorous experimental verifications for several long-sought theoretical predications of aperiodic graphene structures.

PACS: 73.20.At, 73.63.Kv, 31.15.ae, 68.37.Ef

The tremendous efforts devoted to graphene research in the past few years have uncovered numerous extraordinary physical and chemical properties of this material [1-4]. In reality, graphene samples always contain defects that significantly alter graphene's intrinsic properties. Aperiodic structures in which the periodic, hexagonal symmetry is disrupted may bestow new properties and functionalities that are absent in the pristine graphene [5-7]. A famous example is graphene nanoribbons with zigzag edges (ZGNR) – a structure possessing spin-polarized metallic edge states [8-10]. Other examples include localized states associated with point defects [11-13], bandgap opening in GNRs [14-16] and metallic channels provided by defect lines [17, 18], to name a few. Since these new properties may be useful in applications in electronics, chemical reactivity, optical response and spintronics, it has become a major interest to understand the nature of various types of defects. As compared to the numerous theoretical works, experimental studies of the electronic structures of graphene with aperiodic structures are fewer since it is extremely challenging to fabricate samples with well-defined defects while characterizing the electronic structures locally at the defects. Scanning tunneling microscopy (STM) and spectroscopy were used to probe the local density of states of point defects and various edges [19-27]. Detecting the predicated edge states of narrow ZGNRs with atomically sharp and perfect zigzag edges is yet to be achieved. Since the nature of the edge states may depend sensitively on edge morphology, lacking of GNR samples with perfect zigzag edges has hindered the rigorous verification of the theoretical predictions.

Here we demonstrate that various graphene aperiodic structures including GNRs with homogenous and perfect zigzag or armchair edges, single vacancy (SV) or Stone-Wales (S-W) defects and dislocation lines can be created by low-temperature STM manipulation of coronene (top inset in Fig. 1 (a)) molecules on a Cu(111) surface inspired by theory [28] and the

pioneering work of Gomes *et al*[29]. We resolved localization of the edge or point defect states at one of the two sublattices, and the sublattice-specific exponential decay. Our results demonstrate a high degree of control over artificial graphene system that is not possible in real graphene.

Coronene molecules were deposited on a Cu(111) sample held at room temperature. After 120°C annealing, the coronene molecules are random distributed on the Cu(111) surface at 4.8K. Figure 1(a) shows a triangular array constructed by manipulating 300 coronene molecules with an inter-molecular distance of 2.7 nm. Subjected to the repulsive potential provided by the coronene molecules, the two-dimensional electron gas (2DEG) provided by the Cu(111) surface states electrons are confined in the channels of a honeycomb network. The center of the triangle formed by three neighboring molecules can be viewed as the atomic site of the honeycomb structure, whereas the middle bridges between two adjacent molecules corresponds to the "bonds" of the honeycomb structure. Figure 1(b) shows a tunneling spectrum averaged over the artificial graphene, which corresponds to the density of states (DOS). The V-shape DOS is a manifestation of massless Dirac Fermions [28-30]. The bottom of the V, Dirac point, is at 0.23 V below the Fermi level, and is 0.17 V above the onset of the Cu(111) surface state-state band that forms the 2DEG. Furthermore, we resolved the quasiparticle band dispersion using Fourier-transformed scanning tunneling spectroscopy (FT-LDOS, detail see Supplementary Materials). Figure 1(c) shows the power functions in ΓK (left) and ΓM (right) directions. At -0.23 eV, the band structure can be described by a Dirac cone at the K and K' points of the Brillouin zone. Scattering between these Dirac cones give rise to characteristic features in the FT-LDOS spectrum along the ΓK and ΓM directions. We have calculated the band structure by treating the system as a non-interacting 2DEG in a triangular array of repulsive potential disks as illustrated

in the inset of Fig. 1(a) [31]. The potential is set as 1.0 eV, the muffin-tin radius is 0.53 nm, and the effective mass of the Cu surface-state band is $0.4m_e$. The calculated DOS and FT-LDOS are plotted in Fig. 1(b) and (d), respectively. One can see that the experiments and theory agree very well (Note the dashed curves in Fig. 1(c) and (d) highlight the intensity of the calculated FT-LDOS). The Fermi velocity obtained from the band structure is 2.6×10^5 m/s. Note the different potential profiles of the coronene molecules used in our work and the CO molecules used in Ref. 29 should also lead to some differences in the electronic structure of various defects, such as the energy of the defect state or the size of band gaps, etc.

Termination of infinite graphene sheet results in edge(s). Ideal graphene nanoribbons (GNRs) should have two parallel edges. We constructed artificial GNRs of specific configurations. The left part of Fig. 2(a) shows a section of a 6-ZGNR (the full length of the ZGNR is about four times longer containing 40 repeated units and we only consider the data in the middle part in order to minimize the end effects) where the dashed lines are guides for the eye. Since the 2DEG outside the GNR region is depleted by the close-packed molecules, this structure can be viewed as a ZGNR. We define that the bottom edge is of sublattice A and the top edge is of sublattices B, and different rows are numbered from 1 to 6. Row-averaged DOS acquired at the defined rows are plotted in Fig. 2(c). Both edge rows (A1 and B6) have a pronounced peak emerging at Dirac point as marked by the dashed line. The amplitude of the new state as a function of row index is displayed in Fig. 2(d). The amplitude decays in the interior of the ribbon, indicating the state is localized at the two edges. Interestingly, the two sublattices behave independently and each one can be fitted by an exponential function $e^{-L/\xi}$ with a decay constant $\zeta=1.1a_0$ ($1.6\ a_0$) for A (B) sublatticc, where a_0 is the artificial bond length. The localization of the state is apparent in the DOS map, as shown in the left part of Fig. 2(b), which was acquired at the energy of the edge

states (-0.26 V). One can see that the high intensity spots are at the lattice sites of the two edges (A1 or B6). All these features are consistent with the predictions [8-10,14]. We simulated a 6-ZGNR shown in the right part of Fig. 2(a). (The calculated quasiparticle band structure is shown in Supplementary Materials.) The simulated row-averaged DOS, as shown in Fig. 2(c), manifest states (marked by the dashed line) at -0.24 V whose intensity is maximum at the two edges and decays in the interior. The decay trend is plotted in Fig. 2(d), which can be fitted by an exponential function with a decay constant of $1.6a_0$. The simulated real-space DOS map at -0.24 V shown in the right part of Fig. 2(b) further reveals the spatial localization of these states along the two edges. In our measurements, we do not observe any splitting of the edge states arising from magnetic effects [14]; we neglect such effects in our simulations. Overall the simulation nicely reproduces the characteristics of the experimentally-resolved edge states. We also constructed a 4-ZGNR and a 2-ZGNR and found both structures have states that are localized at the two edges (see Supplementary Materials). The single-sublattice behavior of the zero-energy (relative to the Dirac point) edge states of the ZGNRs can be understood by considering the appropriate boundary conditions in $\vec{k} \cdot \vec{p}$ perturbation theory [32]. On a single zigzag edge, the terminal honeycomb sites all belong to a single (B) sublattice. The wavefunction should vanish on the A sites exterior to the ribbon that are adjacent to these terminal B sites. Furthermore, for the zero energy states, the $\vec{k} \cdot \vec{p}$ wavefunction should vanish on all interior A sites as well [32]. The 558 line defect and single vacancy structures we have constructed further illustrate this principle.

For comparison, we constructed a system not expected to show such single-sublattice behavior: an artificial 7-AGNR as shown in the left part of Fig. 2(e). Row-averaged DOS acquired at the defined rows are displayed in Fig. 2(g). In clear contrast to the ZGNRs, the

AGNR does not have any edge states near the Dirac point energy. Figure 2(f) shows a STS map acquired at -0.24 V, which reveals that the states are distributed in the entire ribbon. We simulated the artificial 7-AGNR (right part of Fig. 2(f) (the calculated quaiparticle band structure is shown in Supplementary Materials). As shown in Fig. 2(g), the simulated DOS exhibit comparable features as the experimental ones: a dip at -0.24 V and the absence of any localized edge state. In conclusion, both experimental observations and theoretical simulations confirm that the artificial AGNR does not have the edge states.

Now we turn our focus to line defect. A widely-studied topological line defect consists of repeating paired pentagons fused with octagons, named as 558 line defect [11]. Recently, Lahiri et al. [18] reported on experimental observation of this type of line defect when growing graphene on a Ni substrate. The DFT calculation predicted the existence of metallic states that are localized at the line defect [18]. We made an artificial structure which represents an analogue of 558 line defect. Starting from a perfect triangular coronene molecular structure, we shifted the molecules of the two neighboring columns in a way that four neighboring molecules were pushed together while the molecules in the upper and lower rows were separated apart. This process was repeated along the entire column. Figure 3(a) up panel shows a section of the artificial defect line(the full length is four times larger), where a structural model of the 558 line defect is sketched. We define the center of the two columns as the defect line (DL) and different columns as A^L_n, B^L_n, A^R_n, B^R_n, respectively, where A(B) stands for a sublattice, L(R) for a column to the left (right) of the DL and n the distance index. Column-averaged DOS acquired at the defined columns are plotted in Fig. 3(c). One can see that the V-shape dip disappears at the DL. Interestingly, the spectra at B^L_1 and B^R_1 show a peak at -0.23 V, which indicates that there are new states emerging at Dirac point at the B sublattice. In contrast, the new states are absent at

A sublattice. Figure 3(d) low panel displays the measured dI/dV amplitude at -0.23 V as a function of column index, manifesting (1) the new states are absent in the DL or the A sublattice, (2) in the B sublattice, the amplitude decays away from the DL. In Figure 3(b) up panel, a DOS map acquired at -0.23 V reveals that the new states are confined within four lattice sites in the vicinity of the DL. We simulated the artificial 558 line defect (Fig. 3(a) low part). The calculated column-averaged LDOS spectra are shown in Fig. 3(c). (the calculated quasiparticle band structure is shown in Supplementary Materials). Similar as the experimental observation, at -0.21 V, a new state emerges at B sublattice only but are absent at A sublattice. As shown in Fig. 3(d) up panel, away from the DL, the amplitudes of the new state at B sublattice decays exponentially. A DOS map of -0.21 V is shown in Fig. 3(b) low panel, which reproduces the localization characteristics observed in the experiment. These results confirm that the 558 line defect exhibit states near Dirac point along the line and in particular, the state is only present at the sublattice which borders the line defect.

In the last part, we present the results of two basic types of intrinsic point defects - single vacancies and Stone-Wales defects. It was shown theoretically that vacancies induce quasi-localized states at the Fermi level if the intrinsic electronic structure shows electron-hole symmetry [6]. Experimentally, STM revealed that single vacancies on a graphite surface can introduce a sharp electronic resonance at the Fermi energy around each single graphite vacancy [19-21]. Here, we created a structure by inserting an extra coronene molecule at the center of three adjacent coronene molecules in a regular array. As shown in Fig. 4(a), the extra molecule occupies a lattice site in the honeycomb structure. Since this molecule provides a repulsive potential, this site becomes a barrier for the 2D surface electrons, so this structure can be viewed as an artificial missing-atom defect. We measured the local DOS at the sites that are in specific

distance to the defect denoted as A_n or B_n, where A(B) stands for A(B) sublattice (Note the vacancy is at sublattice B) and n the distance index (n=1 defines the three nearest sites). As shown in the left panel of Fig. 4(b), the two sublattices exhibit very different characters: a measured peak (-0.23 V) appears near Dirac point only at A sites, while the B sites show a V-shape dip. In accordance with the breaking of the A-B sublattice symmetry, the measured dI/dV map (upper panel of Fig. 4(c)) taken at -0.23 V shows that the new state appears at the A sublattice sites only. The dI/dV map further reveals that the new state is localized around the vacancy. To resolve the spatial localization quantitatively, we averaged the spectra of the equivalent sites of A_n and B_n in all radial directions originated from the defect. The results are summarized in Fig. 4(d). One can find two interesting features: (1) the intensity of the new states at A sites decays exponentially, which can be fitted by an exponential function with a decay constant of $1.2a_0$; (2) the intensity is low at B sites and increases slightly away from the vacancy. The symmetry-breaking becomes insignificant beyond tenth lattice site. All these features are explained and quantitatively reproduced by theory as seen in Fig. 4.

Stone-Wales (S-W) defect represents the simplest example of topological defects, in which four hexagons are transformed into two pentagons and two heptagons by rotating a C-C bond by 90° [5, 12,13,33]. This type of defect does not have dangling bonds, but they were predicted to scatter the electron waves strongly and hence have a drastic influence on the electrical transport properties [7]. We made an artificial S-W defect by re-locating four adjacent coronene molecules that are in orthogonal positions as shown in Fig. 4(e). We found that this structure also exhibits a pronounced peak near Dirac point (-0.23 V), as revealed by the site-specific dI/dV acquired at one of the pentagons as shown in the upper panel of Fig. 4(f). For reference, the dI/dV acquired at the black dot in Fig. 4(e) is also plotted, showing a normal V-shape dip. Figure 4(g) (left

panel) is a -0.23 V dI/dV map which manifests that the new states are spatially localized at the two pentagons. We also made several defects with other configurations (see Supplementary Materials). In all these examples, we found that emergence of the localized states near Dirac point is a general phenomenon. We simulated the artificial single vacancy and the SW defects. The results, as shown in Fig. 4(b-d, f and g.), reproduce the experimental-obtained features qualitatively. The defect state decays exponentially with a decay length of 2.1 a_0. The discrepancies of the simulation and the experiment presumably are caused by the simplicity of the muffin-tin type potential used in the simulation.

We expect that the strategy used in this work may be able to create non-trivial states such as 2D topological insulators using potentials with magnetic moment or modulating the surface states that have a strong spin-orbit coupling [34].

This work is supported by the Hong Kong RGC (No. 602712), the National Science Foundation Grant No. DMR 10-1006184 and by the Director, Office of Science, Office of Basic Energy Sciences, Material Sciences and Engineering Division, U.S. Department of Energy under contract No. DE-AC02-05CH11231. S.G.L. acknowledges support from a Simons Foundation Fellowship in Theoretical Physics. We acknowledge the assistance of the XSEDE computational cluster resource provided by NICS (Kraken), supported by the National Science Foundation.

*Correspondence to: phnlin@ust.hk

References:

[1] K. S. Novoselov, *et al.*, Science **306**, 666-669 (2004).

[2] K. S. Novoselov, *et al.*, Nature **438**, 197-200, (2005).

[3] A. H. C. Neto, F. Guinea, N. M. R. Peres, K. S. Novoselov and A. K. Geim, Rev. Mod. Phys. **81**, 109-162 (2009).

[4] A. K. Geim, Science **324**, 1530-1534, (2009).

[5] F. Banhart, J. Kotakoski and A. V. Krasheninnikov, ACS Nano **5**, 26-41 (2010).

[6] V. M. Pereira, F. Guinea, J. M. B. Lopes dos Santos, N. M. R. Peres and A. H. C. Neto, Phys. Rev. Lett. **96**, 036801 (2006).

[7] O. V. Yazyev and S. G. Louie, Phys. Rev. B **81**, 195420 (2010).

[8] M. Fujita, K. Wakabayashi, K. Nakada and K. Kusakabe, J. Phys. Soc. Jpn. **65**, 1920–1923 (1996).

[9] K. Nakada, M. Fujita, G. Dresselhaus and M. S. Dresselhaus, Phys. Rev. B **54**, 17954–17961 (1996).

[10] Y.-W. Son, M. L. Cohen and S. G. Louie, Nature **444**, 347-349 (2006).

[11] R. Faccio, *et al.*, J. Phys. Chem. C **114**, 18961-18971 (2010).

[12] J. Ma, D. Alfè, A. Michaelides and E. Wang, Phys. Rev. B **80**, 033407 (2009).

[13] E. J. Duplock, M. Scheffler and P. J. D. Lindan, Phys. Rev. Lett. **92**, 225502 (2004).

[14] Y. W. Son, M. L. Cohen and S. G. Louie, Phys. Rev. Lett. **97**, 216803 (2006).

[15] S. Dutta and S. K. Pati, J. Mater. Chem. **20**, 8207-8223 (2010).

[16] M. Y. Han, B. Ozyilmaz, Y. B. Zhang and P. Kim, Phys. Rev. Lett. **98**, 206805 (2007).

[17] E. Cockayne, *et al.*, Phys. Rev. B **83**, 195425 (2011).

[18] J. Lahiri, Y. Lin, P. Bozkurt, I. I. Oleynik and M. Batzill, Nat. Nanotechnology **5**, 326-329, (2010).

[19] M. M. Ugeda, I. Brihuega, F.Guinea and J. M. Gómez-Rodríguez, Phys. Rev. Lett.**104**, 096804 (2010).

[20] M. M. Ugeda, *et al.*, Phys. Rev. Lett. **107**, 116803 (2011).

[21] M. M. Ugeda, *et al.*, Phys. Rev. B **85**, 121402 (2012).

[22] C. Tao, *et al.*, Nat. Phys. **7**, 616-620 (2011).

[23] Y. Kobayashi, K. Fukui, T. Enoki and K. Kusakabe, Phys. Rev. B **73**, 125415 (2006).

[24] K. A. Riter and J. W. Lyding, Nat. Materials **8**, 235–242 (2009).

[25] M. Pan, *et al.*, Nano Lett. **12**, 1928–1933 (2012).

[26] X. Zhang, *et al.*, ACS Nano. **7**, 198–202 (2013).

[27] P. Ruffieux, *et al.*, ACS Nano **6**, 6930-6935 (2012).

[28] C.-H. Park and S. G. Louie, Nano Lett. **9**, 1793-1797 (2009).

[29] K. K. Gomes, W. Mar, W. Ko, F. Guinea and H. C. Manoharan, Nature **483**, 306-310 (2012).

[30] Nadvornik, L. *et al.*, New J. Phys. 14, 053002 (2012).

[31] S. Wang, W. Wang, L. Z. Tan, X. Li, Z. Shi, G. Kuang, P. N. Liu, S. G. Louie, N. Lin, Phys. Rev. B. 88, 245430 (2013).

[32] L. Brey and H. A. Fertig, Phys. Rev. B. **73**, 235411 (2006).

[33] B. W. Jeong, J. Ihm and G.-D. Lee, Phys. Rev. B **78**, 165403 (2008).

[34] P**.** Ghaemi**,** S**.** Gopalakrishnan and T. L. Hughes, Phys. Rev. B **86**, 201406 (2012).

FIG. 1 (a) STM image of an artificial pristine grahene structure of a triangular array consisting of 300 coronene molecules. Top inset: chemical structure of coronene; bottom inset: simulation model (the red discs are 1.0 eV potentials). Scale bar: 5 nm (b) Experimental dI/dV (solid) and simulated DOS spectrum (dashed). (c) Power function along □K (left) and □M (right) directions resolved by 2D-FT-LDOS. Dashed curves are simulated band dispersions along the defined directions. (d) Simulated FT-LDOS.

FIG. 2 (a-d) An artificial 6-ZGNR. (a) STM image (left part) and simulation model (right part). (b) STS map acquired at -0.26 V (left part) and simulated LDOS map at -0.24 V (right part). (c) Experimental row-averaged dI/dV spectra and calculated LDOS. Black dashed line indicates Dirac point. (d) The amplitude of the edge state (We use the term "amplitude of the edge state" to refer to the modulus-squared of the wavefunction in the calculation, and to the dI/dV value at the position and bias voltage of the edge state in the experiment.) as a function of row index. Experimental (calculated) results are shown in solid (open) symbols. (e-g) An artificial 7-AGNR. (e) STM image (left part) and simulation model (right part). (f) STS map acquired at -0.23 V. (g) Experimental row-averaged dI/dV spectra and calculated LDOS. Scale bars: 5 nm.

FIG. 3 (a) STM image (up part) and simulation model (low part) of an artificial 558 defect line. (b) STS map acquired at -0.23 V (up part) and simulated LDOS map at -0.21 V (right part). (c) Experimental column-averaged dI/dV spectra and calculated LDOS. (d) Calculated LDOS intensity (up panel) measured LDOS amplitude (low panel) at -0.22 V as a function of column index. Scale bars: 5 nm.

FIG. 4. (a-d). An artificial single vacancy. (a) STM image. (b) Experimental (up) and simulated (low) dI/dV spectra acquired at sites A_1 and B_1 (marked as the black and red dots in (A)). (c) Experimental (up) and simulated (low) dI/dV maps at -0.23 V. (d) Experimental (solid) and simulated (empty) -0.23 V LDOS amplitude as a function of sites. (e-g). An artificial Stone-Wales defect. (e) STM image. (f) Experimental (up) and simulated (low) dI/dV spectra (Red: acquired with the tip located at the red dot marked in (e); Black: from the un-modified sites). (g) Experimental (left) and simulated (right) dI/dV maps at -0.23 V. Scale bars: 5 nm.

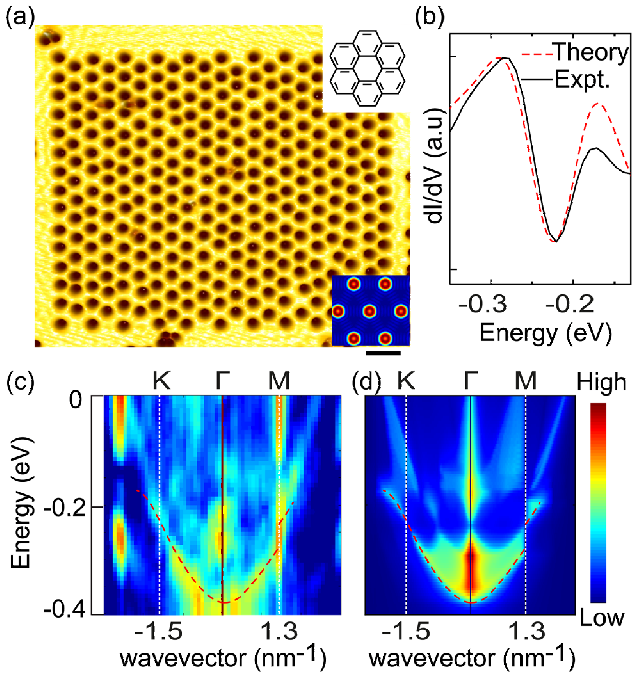

Figure 1 LK14279 13OCT2014

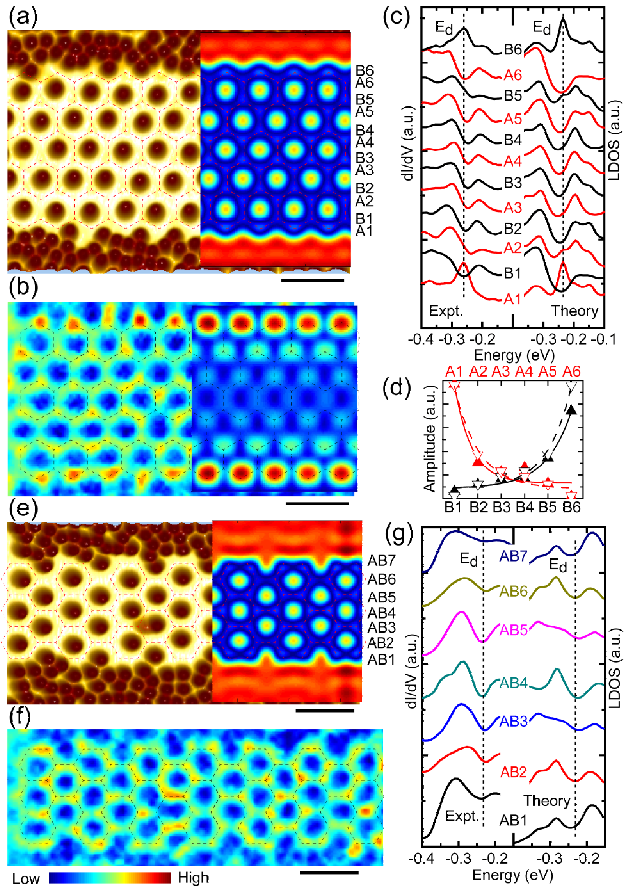

Figure 2 LK14279 13OCT2014

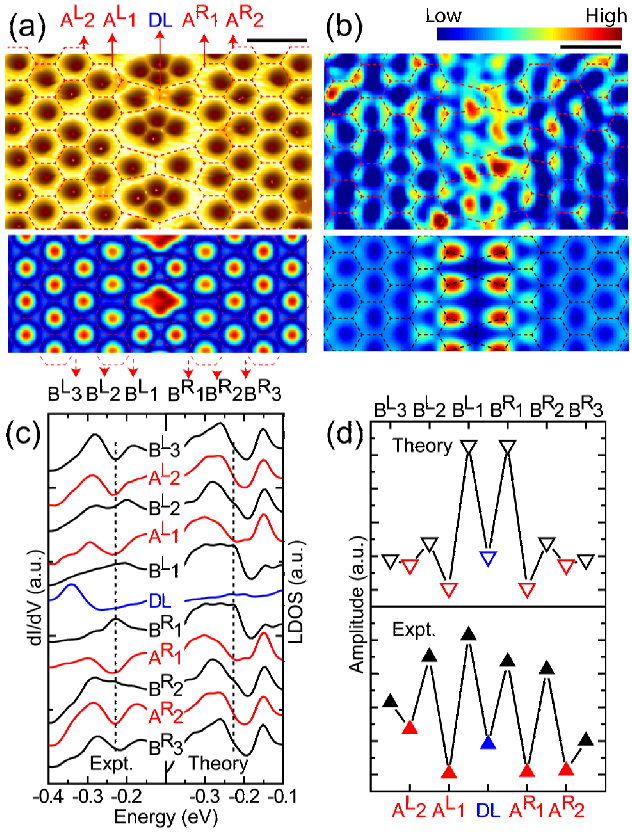

Figure 3 LK14279 13OCT2014

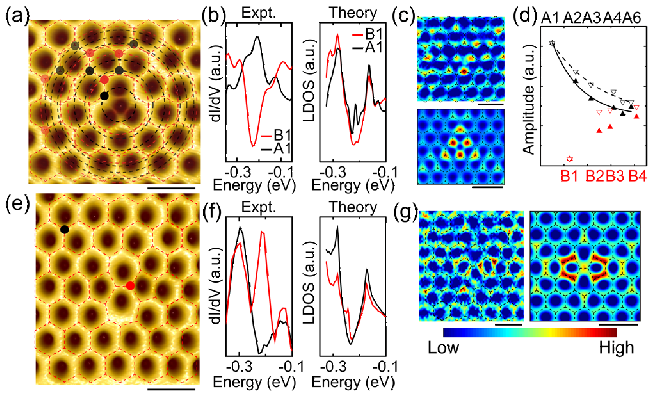

Figure 4 LK14279 13OCT2014